# Numerical Derivation of Steady Flows in Visco-resistive Magnetohydrodynamics for JET and ITER-like Geometries with no Symmetry Breaking

H Oueslati, T Bonnet, N Minesi, Marie-Christine Firpo, A. Salhi

## To cite this version:

H Oueslati, T Bonnet, N Minesi, Marie-Christine Firpo, A. Salhi. Numerical Derivation of Steady Flows in Visco-resistive Magnetohydrodynamics for JET and ITER-like Geometries with no Symmetry Breaking. AIP Conference Proceedings, 2019, ⟨10.1063/1.5135482⟩. ⟨hal-02379461⟩

# Numerical Derivation of Steady Flows in Visco-resistive Magnetohydrodynamics for JET and ITER-like Geometries with no Symmetry Breaking

H. Oueslati,$^{1,2}$ T. Bonnet,$^{1}$ N. Minesi,$^{1}$ M.-C. Firpo,$^{1,\text{a)}}$ and A. Salhi$^{2}$

$^{1)}$*Laboratoire de Physique des Plasmas, CNRS, Ecole Polytechnique, 91128 Palaiseau cedex, France*
$^{2)}$*Département de physique, Faculté des Sciences, Université de Tunis el Manar, Tunisie*

$^{\text{a)}}$*Corresponding author: firpo@lpp.polytechnique.fr*

**Abstract.** Plasma rotation proves to have important effects on the improvement of the confinement and on the entrance into the H-mode of improved confinement in tokamaks. To consider this issue, we propose to determine numerically the steady states of the visco-resistive MHD equations including the non-linear $(\mathbf{v}.\nabla)\mathbf{v}$ term. We take into account the external electric field in the toroidal direction used to create the toroidal current required in a tokamak to create the poloidal component of the magnetic field. Numerical results in JET and ITER geometries obtained using the finite element programming language FreeFem++ are presented. We consider realistic values of the resistivity $\eta$ and vary the viscosity, $\nu$, of which the realistic order of magnitude is poorly known. The axisymmetric steady-state visco-resistive MHD equations with symmetric boundary conditions are solved using a continuation method on $\nu$ and a Newton-Raphson scheme to handle the nonlinearity.

## INTRODUCTION

The original theoretical approach to assess the viability of the machine configurations for magnetic confinement fusion has been to consider steady-state motionless magnetohydrodynamic (MHD) equilibria and derive their linear theory, namely study their stability with respect to small perturbations. Some reason for this was also that, in the presence of equilibrium flows, the stability of fluids and plasmas remains a difficult issue from an analytical point of view [1]. In terms of the modeling framework, because nonideal terms, such as in particular resistive terms, however small they are, modify the structure of the MHD equations, it is not surprising that nonideal MHD steady-states are different from the ideal ones. Therefore, as far as steady-states are concerned, the realistic approach should consider inherently non-ideal MHD equations instead of the ideal ones.

The geometry has also proven to be important. Whereas in cylinder geometry there are resistive steady states with zero velocity, which form the basic class of equilibria from which classical linear theory is derived, it happened that these zero velocity states cannot survive the introduction of toroidal effects [2]. In truly toroidal conditions, resistive steady states possess non-zero steady flows. Montgomery and co-workers have notably pointed out this discrepancy and have conducted a research program to characterize the realistic non-ideal steady states in toroidal geometry. In Ref. [3], Kamp and Montgomery considered the visco-resistive MHD equations in toroidal geometry and were able to compute the associated steady-states using some meaningful assumptions. The aim of the present study is to follow this path and investigate the steady-state MHD velocity field associated to realistic values of the resistivity, $\eta$, and to realistically small values of the viscosity, $\nu$, (up to two orders) below the lowest value considered in [3]. A central objective here is to figure out the sensitivity of the magnitude of the toroidal velocity field on the viscosity.

The first section is devoted to the introduction of the model equations and their boundary conditions. The second section addresses the implementation of the later system of partial differential equations into the finite element programming code FreeFem++ beginning with its weak formulation. The third section presents a validation study of our numerical code through a comparison against simulation results obtained with FEMLAB in Ref. [3]. Then, the framework and the simulation results obtained in JET and ITER geometries are presented in the fourth section. Conclusions and perspectives of the study are finally addressed.

## The system of equations

We shall first introduce the minimal mathematical frame necessary to compute visco-resistive MHD steady states allowing for non-vanishing velocity fields. The physical unknown quantities are the electric field $\mathbf{E}$, the magnetic field $\mathbf{B}$, the velocity field $\mathbf{v}$ and the scalar pressure $p$. The conducting plasma fluid is assumed to have a uniform

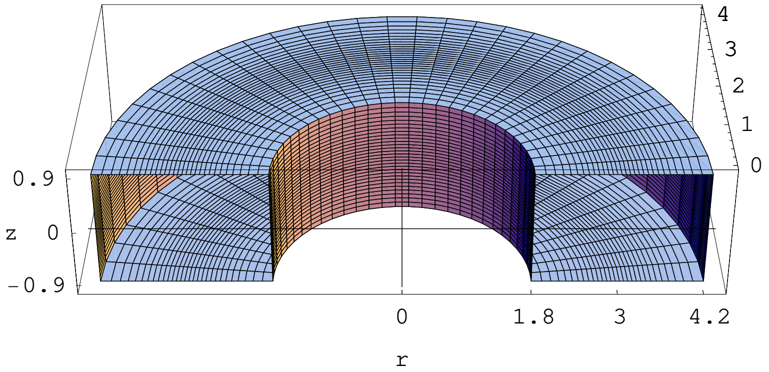

**FIGURE 1.** Geometry of the toroid used in the computations of the third section. The length unit is the meter.

density so that the mass conservation equation amounts to write the incompressibility condition (1b). The steady-state Navier-Stokes equation normalized to the mass density, $\rho$, is written in Eq. (1a). These fluid equations are coupled to the Maxwell equations (1c)-(1d)-(1e) and to the Ohm's law (1f) written for dimensionless variables in the usual Alfvèn units where velocities are normalized by the characteristic Alfvèn velocity $v_A = (B^2/\mu_0\rho)^{1/2}$.

The full system of equations reads

$$(\mathbf{v}.\nabla)\mathbf{v} = \mathbf{J}\times\mathbf{B} - \nabla p + \nu\nabla^2\mathbf{v} \tag{1a}$$

$$\nabla.\mathbf{v} = 0 \tag{1b}$$

$$\nabla.\mathbf{B} = 0 \tag{1c}$$

$$\nabla\times\mathbf{E} = 0 \tag{1d}$$

$$\nabla\times\mathbf{B} = \mathbf{J} \tag{1e}$$

$$\mathbf{E} + \mathbf{v}\times\mathbf{B} = \eta\mathbf{J}. \tag{1f}$$

There are two (small) dimensionless parameters in this system, that are the resistivity $\eta$, which is the inverse of the magnetic Reynolds number $S$, and the kinematic viscosity $\nu$, which is the inverse of the viscous Lundquist number $M$. One may introduce another (large) parameter from the combination of $S$ and $M$, such as the Hartmann number $H$ defined through $H = \sqrt{MS}$. Here the modeling of the resistive effects has been made in the (usual) scalar way. In the steady Navier-Stokes equation (1a), the viscosity has also been assumed to be scalar. The system (1) needs now to be completed by the specification of the problem geometry and boundary conditions.

Since our interest lies in toroidal magnetic confinement devices for fusion, we shall consider cases where the plasma fluid is confined within a toroid. In order to probe our computations against Kamp and Montgomery's results [3], we shall consider in the first place a torus with rectangular cross-section having the same parameters as in Ref. [3], namely a major radius of 3 meters, a 1.8 meters height and 2.4 meters length. This schematic geometry is represented in Figure 1. Later in the article, we shall consider the realistic cases of JET and ITER-like geometries. Moreover, we shall restrict to the two-dimensional problem by imposing axisymmetry.

Computationally convenient and idealized boundary conditions are chosen as in Ref. [3]. Namely, we shall assume that the tokamak walls are ideally conducting so that the normal component of the magnetic field should vanish at the walls. As for the velocity field, it will be assumed as in the hydrodynamics of neutral fluids that its normal component to the walls also vanishes, although this classical condition may not be accurate for plasmas. An identical assumption will be made for the current density. Additionally, it is imposed that any tangential viscous stress vanishes at the vessel walls.

Tokamaks are mostly driven devices and this must be taken into account in the modeling. Each discharge starts by inducing an electric field in the toroidal direction. This serves first to create the plasma by ionizing the gas in the vacuum chamber and then to drive the toroidal current that generates and sustains the poloidal magnetic field. Since our approach is steady-state, there is an implicit assumption here that the visco-resistive MHD dynamical timescales are negligible compared with the typical duration of a discharge. Indeed, even if during a discharge, some change in the plasma parameters may occur in time, because the timescales of the energy and current diffusion are much longer than the MHD timescales (Alfvèn transit time), one may consider that the plasma evolves through successive static MHD steady-states which validates the present approach. As in Ref. [3], the expression of the external electric field will be

$$\mathbf{E}_{\text{ext}} = E_0 \frac{r_0}{r} \widehat{\mathbf{i}}_\varphi, \tag{2}$$

where $E_0$ just denotes the value of $E_{\text{ext}}$ at the major radius $r_0$. The magnetic field also comprises an external part created by the external poloidal coils of the form

$$\mathbf{B}_{\text{ext}} = B_0 \frac{r_0}{r} \widehat{\mathbf{i}}_\varphi. \tag{3}$$

## Formulation in terms of scalar potentials

From now on, we restrict to the axisymmetric two-dimensional problem and impose the independence of the fields with respect to the toroidal angle $\varphi$. Since the velocity and magnetic fields are solenoidal vector fields (i.e. having zero divergence), there exist scalar fields $\psi$ and $\chi$, respectively called the stream function and the magnetic flux function, such that

$$\mathbf{v}(r,z) = \nabla\psi \times \nabla\varphi + v_\varphi \widehat{\mathbf{i}}_\varphi, \tag{4a}$$

$$\mathbf{B}(r,z) = \nabla\chi \times \nabla\varphi + (B_0 \frac{r_0}{r} + B_\varphi) \widehat{\mathbf{i}}_\varphi. \tag{4b}$$

Moreover, the full expression of the static electric field is the sum of the external field (2) and of the electrostatic part deriving from the gradient of some scalar potential $\Phi$

$$\mathbf{E} = E_0 \frac{r_0}{r} \widehat{\mathbf{i}}_\varphi - \nabla\Phi. \tag{5}$$

The vorticity and the current density fields are respectively defined by $\boldsymbol{\omega} = \nabla \times \mathbf{v}$ and $\mathbf{J} = \nabla \times \mathbf{B}$. Using the previous expressions in Eq. (4), they may be written as

$$\mathbf{J}(r,z) = \nabla(rB_\phi) \times \nabla\phi - \frac{1}{r}(\triangle^* \chi) \widehat{\mathbf{i}}_\varphi \tag{6a}$$

$$\boldsymbol{\omega}(r,z) = \nabla(rv_\phi) \times \nabla\phi - \frac{1}{r}(\triangle^* \psi) \widehat{\mathbf{i}}_\varphi \tag{6b}$$

where the second-order elliptic operator $\triangle^*$ is defined by

$$\triangle^* A = \nabla^2 A - \frac{2}{r}\frac{\partial A}{\partial r} = \frac{\partial^2 A}{\partial^2 r} - \frac{1}{r}\frac{\partial A}{\partial r} + \frac{\partial^2 A}{\partial^2 z}. \tag{7}$$

Let us define the rescaled variables $x = r/r_0$, $y = z/r_0$ and introduce the same notations as in Ref. [3], namely

$$u_1 = \frac{\psi}{r_0} \tag{8a}$$

$$u_2 = r_0 r \omega_\varphi \tag{8b}$$

$$u_3 = \frac{rB_\varphi}{I_b} + 1 \tag{8c}$$

$$u_4 = \frac{rv_\varphi}{I_b} \tag{8d}$$

$$u_5 = \frac{\chi}{r_0} \tag{8e}$$

$$u_6 = r_0 r J_\varphi - I_e \tag{8f}$$

where $I_b = r_0 B_0$ and $I_e = r_0^2 E_0/\eta$. Let us define the Poisson bracket of two functions $u$ and $v$ with respect to the variables $x$ and $y$ as

$$\{u,v\} = \frac{\partial u}{\partial x}\frac{\partial v}{\partial y} - \frac{\partial u}{\partial y}\frac{\partial v}{\partial x}. \tag{9}$$

The system of equations to be solved reads finally

$$\triangle^* u_1 = -u_2 \tag{10a}$$

$$\nu \triangle^* u_2 = \frac{I_b^2}{x^2}\frac{\partial u_3^2}{\partial y} - 2\frac{u_6 + I_e}{x^2}\frac{\partial u_5}{\partial y} \tag{10b}$$

$$+\frac{1}{x}(\{u_6,u_5\}+\{u_1,u_2\}) + 2\frac{u_2}{x^2}\frac{\partial u_1}{\partial y} - I_b^2 \frac{\partial}{\partial y}(\frac{u_4^2}{x^2}) \tag{10c}$$

$$\eta \triangle^* u_3 = \frac{2}{x^2}(u_3\frac{\partial u_1}{\partial y} - u_4\frac{\partial u_5}{\partial y}) + \frac{1}{x}(\{u_1,u_3\}+\{u_4,u_5\}) \tag{10d}$$

$$\nu \triangle^* u_4 = \frac{1}{x}(\{u_3,u_5\}+\{u_1,u_4\}) \tag{10e}$$

$$\triangle^* u_5 = -u_6 - I_e \tag{10f}$$

$$\eta u_6 = \{u_5,u_1\} \tag{10g}$$

in which the operator $\triangle^*$ has to be taken in the new variables $x$ and $y$ as

$$\triangle^* \equiv \frac{\partial^2}{\partial x^2} - \frac{1}{x}\frac{\partial}{\partial x} + \frac{\partial^2}{\partial y^2} = \triangle - \frac{1}{x}\frac{\partial}{\partial x}. \tag{11}$$

## NUMERICAL RESOLUTION WITH THE FINITE ELEMENT METHOD (FEM) USING FREEFEM++

In the present study, the previous non-linear system of equations (10) is solved under its weak formulation using FreeFem++ [4] with the finite element method.

We define by $\Omega \subset \mathbb{R}^2$ the computational domain, that will be the cross-section of the tokamak under consideration, with boundary $\partial\Omega$ and exterior unit normal $\mathbf{n}$. We introduce the function space $V_g$ through

$$V_g = \{u \in H^1(\Omega); u = g \text{ on } \partial\Omega\} \tag{12}$$

Multiplying each line of (10) by any test function $v_i$ in the Hilbert space $H_0^1(\Omega) = V_0$ with the assumption that $v_i|_{\partial\Omega} = 0$, the weak formulation of equations (10) is of the form [5], for all $i = 1,\ldots,5$,

$$\int_\Omega \nabla u_i.\nabla v_i d\Omega + \int_\Omega \frac{1}{x}\frac{\partial u_i}{\partial x} v_i d\Omega + \int_\Omega g_i(\mathbf{u}) v_i d\Omega = 0, \tag{13a}$$

$$\int_\Omega [u_6 - g_6(\mathbf{u})] v_6 \, d\Omega = 0, \tag{13b}$$

with $g_6(\mathbf{u}) \equiv \eta^{-1}\{u_5,u_1\}$. In Eqs. ((13)), we have made use of the Green's formula

$$\int_\Omega -\triangle u v d\Omega = \int_\Omega \nabla u \cdot \nabla v d\Omega - \int_{\partial\Omega} \mathbf{n} \cdot \nabla u v ds. \tag{14}$$

The nonlinearity of the MHD system of equations is contained in the $g_2$, $g_3$, $g_4$ and $g_6$ functional forms. In order to tackle these nonlinear partial differential equations discretized with finite elements, Newton-Raphson's method has been implemented.

The above system of equations ((13)) can be cast under the form $F(\mathbf{u}) = 0$. In order to find the solution $\mathbf{u}$ such that $F(\mathbf{u}) = 0$, the Newton-Raphson's iterative method uses the property that, in the vicinity of $\mathbf{u}$, a Taylor expansion of $F$ yields $F(\mathbf{u}+h) - hDF(\mathbf{u}) = O(h^2)$. Here $DF$ is the differential of $F$ that should be evaluated. An initial guess $\mathbf{u} = \mathbf{u}_0 \in \prod_{k=1,\ldots,6} V_{g_i}$ must be close enough to the solution $\mathbf{u}$ to ensure a good convergence of the algorithm. Defining by $\varepsilon$ the desired accuracy of the Newton-Raphson method, we operate the iteration

- Choose $\mathbf{u}_0$;

```
- For ($i = 0, \ldots, imax$; $i = i + 1$) do
    $\delta_i = F(\mathbf{u}_i)/DF(\mathbf{u}_i)$;
    $\mathbf{u}_{i+1} = \mathbf{u}_i - \delta_i$;
    Break for $\|\delta_i\| < \varepsilon$.
```

As for the implementation of the FEM, FreeFem++ generates automatically the triangulation ($\tau_h$), with $h$ the mesh size. The automatic mesh generation is based on the Delaunay-Voronoi algorithm. For a good mesh generation, it is essential to define the appropriate finite element space. A comparison between P1 and P2 space elements was tested for different meshes. We shall consider this for the results obtained in the ITER geometry. Finally, the boundary $\partial\Omega$ is described analytically by a parametric equation for JET and ITER geometries.

## BENCHMARKS OF THE CODE

The system of partial differential equations governing the driven visco-resistive MHD steady-states relevant to tokamaks and the boundary conditions at the walls have been presented above. We have used FreeFem++ [4] to derive numerically the (weak) solution of this system written in a variational form of the type $F(\mathbf{u}) = \int_\Omega f(\mathbf{u}) \cdot \mathbf{v} d\Omega = 0, \forall \mathbf{v}$ as presented before. We have used a local linearization through a Newton-Raphson algorithm to iteratively find the solution $\mathbf{u}$ providing a very quick convergence.

Our first objective has been to compare our FreeFem++ numerical results with that obtained by Kamp and Montgomery in Ref. [3] using the FEMLAB solver (now called COMSOL). These test-bed results are presented in this Section. For this purpose, we shall set here the parameters $E_0$, $B_0$ and $\eta$ equal to one as in Ref. [3]. The only free parameter remains the viscosity $\nu$ or equivalently the Hartmann number, $H$, which is chosen to be the control parameter. In this Section, the tokamak is modeled as in Ref. [3] by a torus with a rectangular cross-section $\partial\Omega$ with a major radius of 3 meters, a 1.8 meters height and 2.4 meters length, as represented in Figure 1. The boundary conditions imposed upon the solutions of the set of Eqs. (10) are that any tangential viscous stress, and the normal components of $\mathbf{v}$, $\mathbf{J}$, and $\mathbf{B}$, should vanish at the walls.

Below are reproduced some of our numerical results to be compared with the FEMLAB results of Ref. [3] for identical conditions. Figure 2 represents a color plot of the toroidal velocity field $v_\varphi$ in the upper half-part of the cross-section of the toroid. This has to be compared with the Figure 6(b) of Ref. [3] to which it finely agrees.

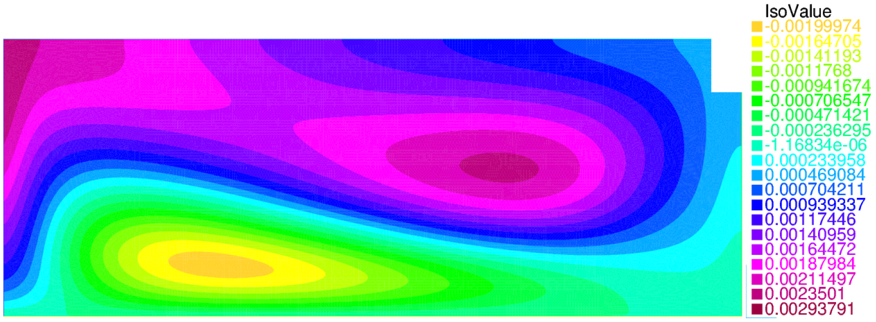

**FIGURE 2.** Toroidal component of the plasma velocity field across the $z \geq 0$ part of the rectangular cross-section in the geometry represented on Fig. 1 for $H = 40$. Other parameters are set to $E_0 = B_0 = \eta = 1$.

Similar agreements can be checked for the case $H = 100$ in Figure 3 to be compared with Figure 7(b) of Ref. [3] and $H = 500$ in Figure 4 to be compared with Figure 8(b) of Ref. [3]. The velocity field is antisymmetric with respect to the $z = 0$ midplane.

Eventually, our simulations were also tested against some scalings derived analytically [6] in the infinite viscosity limit, corresponding here to the $H \to 0$. In this limit, for a given $\eta$, the quadratic means (or root mean squares) of the poloidal and toroidal velocities have been predicted to respectively scale with $H^2$ and $H^4$. This agrees with our numerical results. In particular, Figure 5 represents the behavior of the root mean square (rms) poloidal speed as a function of the Hartmann number. This reasonably strong correlation between the simulations and the theory achieved to provide some solid arguments for the validity of our FreeFem++ numerical code. This concludes the present section devoted to the numerical assessment of our numerical scheme.

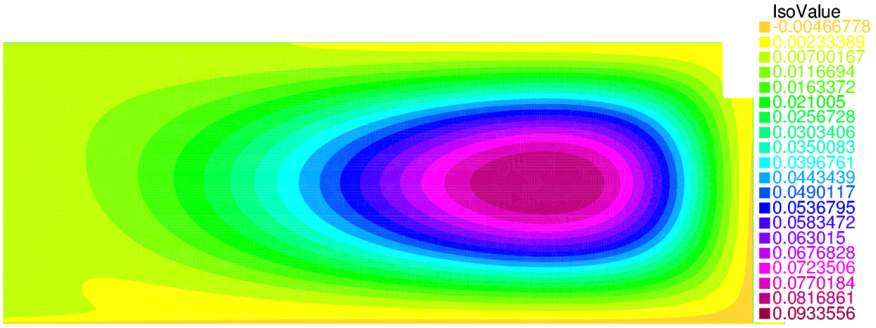

**FIGURE 3.** Toroidal component of the plasma velocity field across the $z \geq 0$ part of the rectangular cross-section in the geometry represented on Fig. 1 for $H = 100$. Other parameters are set to $E_0 = B_0 = \eta = 1$.

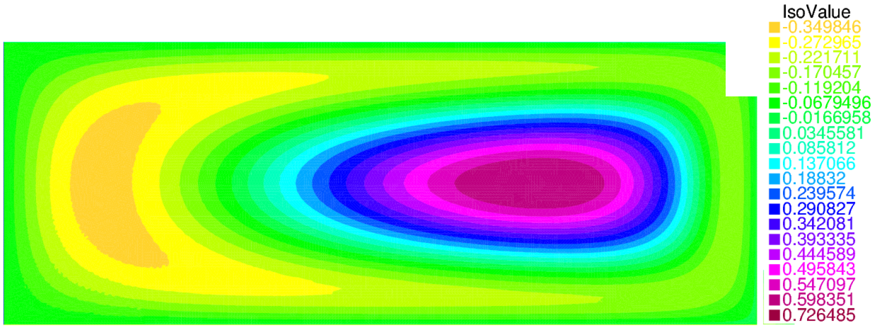

**FIGURE 4.** Same as in Figs. 2 and 3 for $H = 500$.

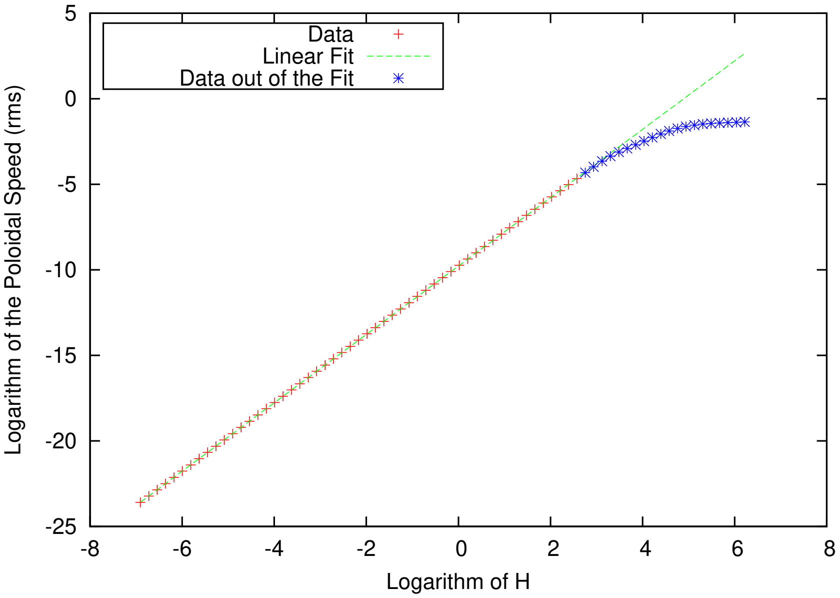

**FIGURE 5.** Poloidal rms speed as a function of $H$ in log-log scale. The fit, done with the algorithm of the gnuplot software [7], has an equation of $y = ax + b$ where $a = 1.99858 \pm 0.00031$ and $b = -9.7799 \pm 0.0011$ for a reduced chi-squared of $4.0 \times 10^{-5}$. The theoretical calculation [6] predicts $a = 2$.

In order to address physically relevant conditions for the magnetic confinement fusion, we shall now change the problem geometry by turning to a JET and ITER-like toroids and by introducing and discussing the operational physical orders of magnitude.

## NUMERICAL DERIVATION OF AXISYMMETRIC STEADY FLOWS FOR JET AND ITER-LIKE GEOMETRIES

### Framework

We turn now to realistic geometries for the JET and ITER tokamaks, as depicted in Figure 6. The equations modeling the boundaries $\partial\Omega$ of these tokamaks read

$$\begin{aligned} x &= \left(1+\frac{r_1}{r_0}\cos(\theta+\arcsin\delta\sin\theta)\right)\cos\varphi, \\ y &= \left(1+\frac{r_1}{r_0}\cos(\theta+\arcsin\delta\sin\theta)\right)\sin\varphi, \\ z &= \frac{r_2}{r_0}\sin\theta, \end{aligned} \tag{15}$$

for $(\varphi,\theta)\in[0;2\pi]^2$. Here $r_0$ is the major radius, $r_1$ the semi-minor axis and $r_2$ the semi-major axis of the cross-section, and $\delta$ the triangularity parameter.

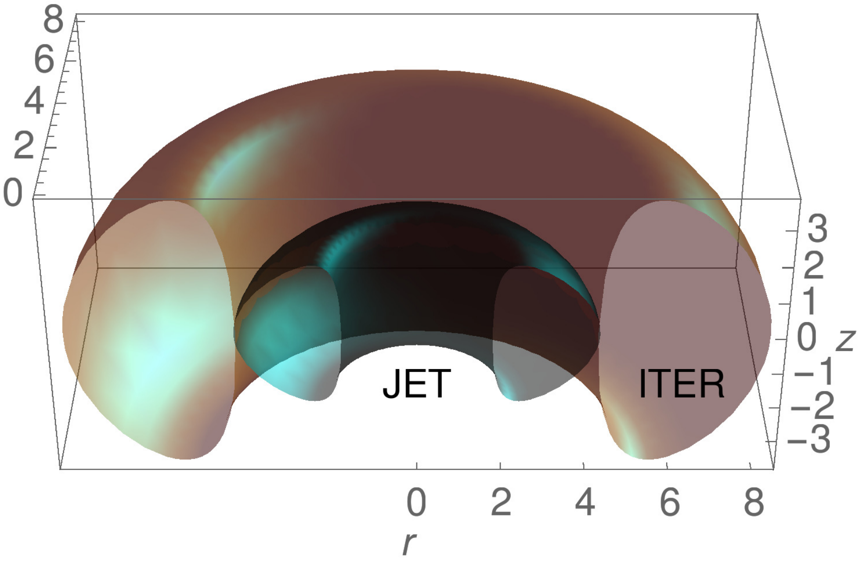

**FIGURE 6.** Geometries of the JET and ITER tokamaks.

We wish to investigate steady flow velocities for realistically large values of the Hartmann number. Because the visco-resistive MHD system of equations is nonlinear and in order to ensure the convergence of the Newton-Raphson iterative procedure, we perform a continuation method starting from a low Hartmann number. The steady-state solution for some Hartmann number $H_j$ serves as an initialization for the Newton-Raphson method for the next Hartmann number $H_{j+1} > H_j$ in this incremental process.

FreeFem++ uses a variety of triangular finite elements (linear and quadratic Lagrangian elements, discontinuous P1, piecewise quadratic P2, Raviart-Thomas elements, etc...) to solve partial differential equations in two dimensions. The present code used to determine the velocity profiles in the toroidal and the poloidal directions of the torus, uses P2 finite element, with mesh adaptivity on the border. Numerically, we use mesh refinement in order to have an optimal convergence of the solutions which becomes critical for large Hartmann numbers when boundary layers form. The approximative solution is associated to a mesh with size $h_i, i = 1, ..., n_i$ and associated finite elements at order 2. In our cases, an initial mesh size of $h_{min} = 0.004$ is considered. Figure 7 represents the adapted mesh used in the JET computations.

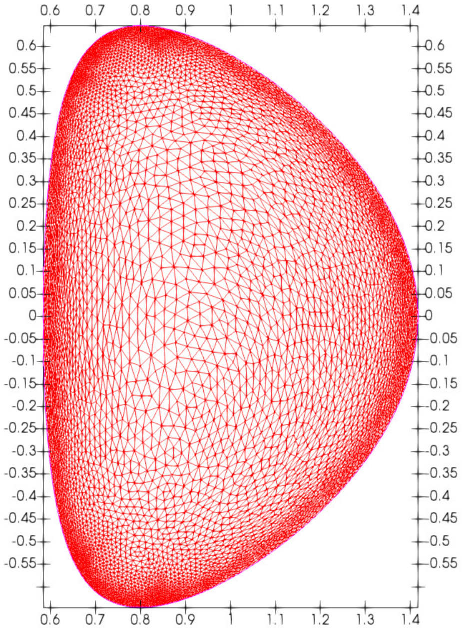

**FIGURE 7.** Representation in the $x$ and $y$ variables of the mesh adaptation on the border for the JET tokamak. Here the number of triangles is 11142, the number of vertices is 5765.

## Velocity fields for realistic JET parameters with symmetric no-slip boundary conditions

The numerical derivation of steady states in visco-resistive MHD in tokamaks requires a high spatial resolution. Toroidal velocities are computed for increasing Hartmann numbers using no-slip boundary conditions.

Typical JET parameters have been taken: the major radius is $r_0 = 3$m, the semi-minor axis radius $r_1 = 1.25$m, the plasma elongation $\kappa = r_2/r_1 = 1.55$ and triangularity is such that $\arcsin\delta = 0.5$. The value of the external toroidal magnetic field $B_0$ is taken to be 2.8T. The toroidal loop voltage is chosen to be equal to 1 Volt. This is a reasonable assumption since the toroidal electric field $E_0$ is of the order of some V.m$^{-1}$ in the present devices [8]. In dimensionless units, the corresponding parameters are $B_0 = 0.87$ and $E_0 = 3.10^{-9}$. Plasma resistivity decreases strongly with temperature as $T^{-3/2}$ (Spitzer's law [9]). In the present simulations, resistivity was fixed to the value $\eta = 6.9 \times 10^{-8}$. Velocities are expressed in Alfvénic units with a JET-relevant Alfvén velocity $v_A = 3.10^6$m.s$^{-1}$.Velocities are expressed in Alfvénic units with a JET-relevant Alfvén velocity $v_A = 3.10^6$m.s$^{-1}$. The evolution as a function of the Hartmann number of the toroidal flow in JET is presented in the Figures 8, 9, 10 and 11.

The topology of the poloidal velocity field for the realistic parameters mentioned before and the Hartmann numbers $H = 10$ and $H = 10^5$ is shown in Figs. 12 and 13.

Finally, the maximal toroidal velocity has been computed as a function of the Hartmann number for two values of the resistivity: $\eta = 6.9 \times 10^{-8}$ and $6.9 \times 10^{-7}$. This is shown on Figure 14.

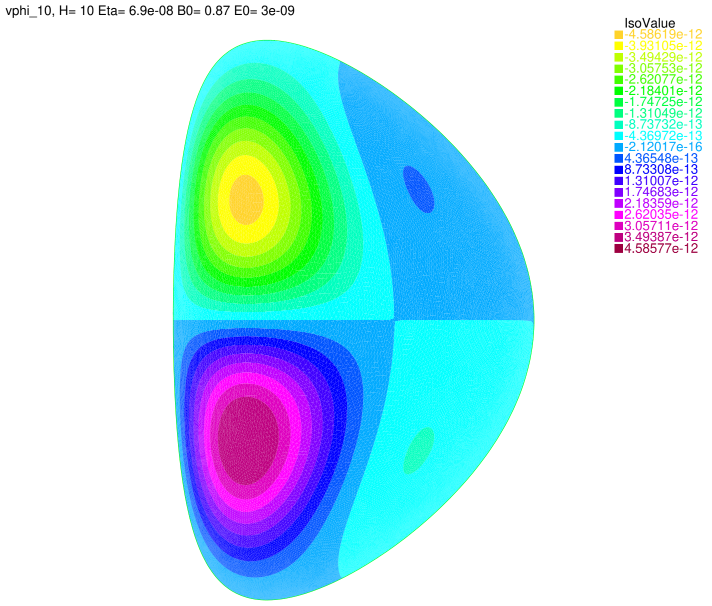

**FIGURE 8.** Toroidal velocity field computed with P2 elements for JET configuration for $H = 10$ with mesh adaptivity on the border. Dimensionless parameters are $E_0 = 3.10^{-9}$, $B_0 = 0.87$ and $\eta = 6.9 \times 10^{-8}$.

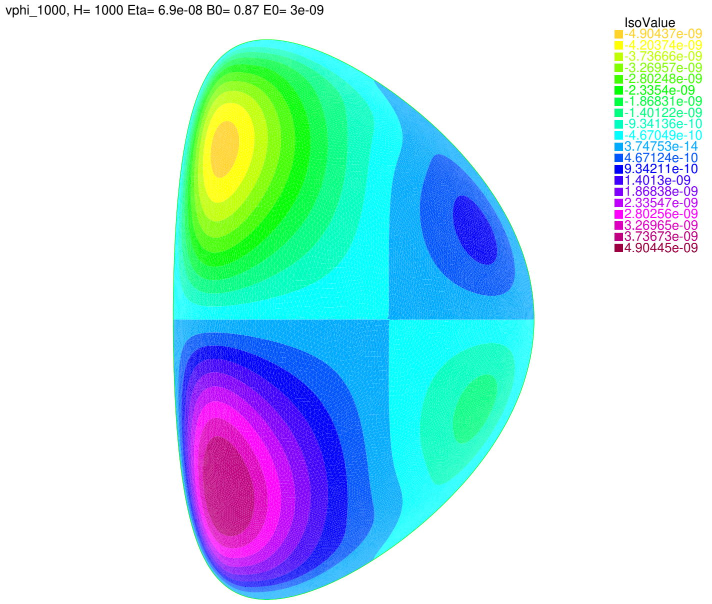

**FIGURE 9.** Same as Fig. 8 for $H = 1000$.

## Numerical results for ITER like-Geometry and comparison with JET

Here the realistic ITER geometry is considered [10]. The toroidal cross-section amounts then to a D-shaped ellipse. Indeed the non-circular, shaped, cross-section was found to be an optimum configuration to reach higher $\beta$ and plasma current in tokamaks. We are thus simulating on the basis of an ellipsoidal section (semi-minor axis of $r_1 = 2$ meters and semi-major axis of $r_2 = 3.7$ meters) of a $r_0 = 6.2$ meters major radius torus. The ITER's triangularity is set to $\delta = 0.33$. Whereas the JET tokamak was able to produce 16 MW of fusion power from a total input heating power

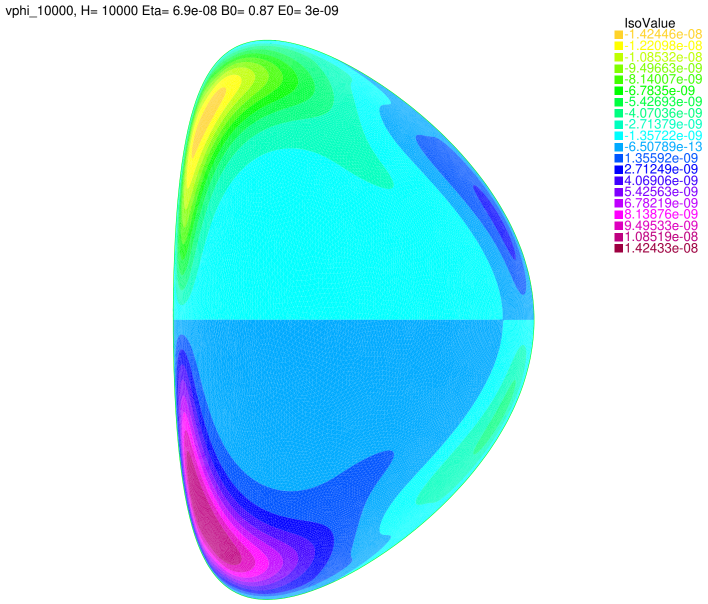

**FIGURE 10.** Same as Fig. 8 for $H = 10^4$.

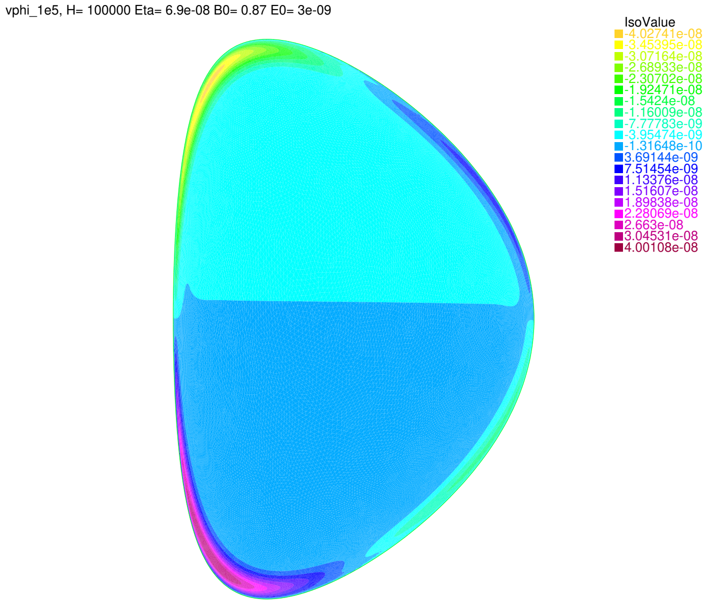

**FIGURE 11.** Same as Fig. 8 for $H = 10^5$.

of 24MW ($Q = 0.67$), ITER is designed to produce a ten-fold return on energy ($Q = 10$), so as to become the first of fusion experiments to produce net energy gain.

The computational domain is larger for ITER than for JET (see e.g. Figure 6). We shall see now that this makes FreeFem++ computations more challenging for ITER than for JET and begin to stress the necessity to use P2 elements instead of P1 to access robust numerics at large Hartmann numbers.

The weak formulation of visco-resistive MHD system of equations is computed with P1 and P2 elements. The P1 elements involve the space of globally continuous affine functions, and denotes the vector space of polynomials of one degree of freedom, with two local nodes associated with piecewise linear basis functions. P2 elements involve

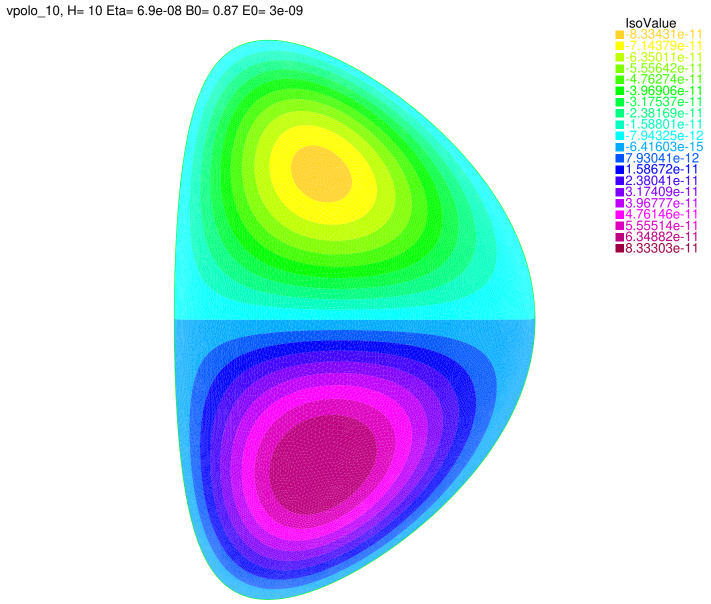

**FIGURE 12.** Poloidal velocity field computed with P2 elements in JET for the same parameters for $H = 10$.

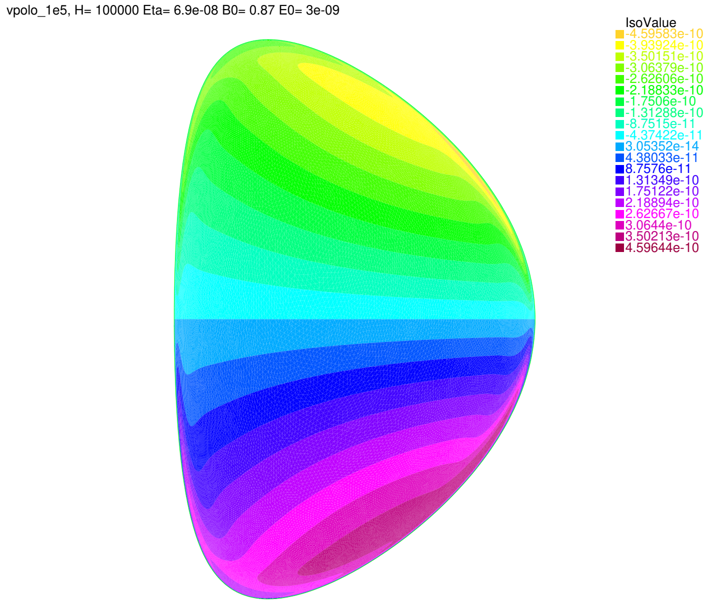

**FIGURE 13.** Same as Fig. 12 for $H = 10^5$.

the space of continuous, piecewise parabolic functions for quadratic elements with three local nodes. As FreeFem++ uses an unstructured triangular mesh defined from the border of the domain, to define the elements P2, one must first introduce the middle points of the triangle segments. We notice clearly the difference of taking higher-order polynomials elements by comparing Figures 15 and 16. The property of anti-symmetry with respect to the equatorial plane of the velocity field is recovered for computations using P2 elements whereas P1 computations become mesh-dependent, and therefore non-robust, for $H \gtrsim 10^4$.

Simulations were performed for different values of $H$, with dimensionless parameters $E_0 = 3.10^{-9}$ and $\eta = 6.9 \times 10^{-9}$, and $B_0 = 5$T. As in the JET case, realistic viscosity is uncertain within orders of magnitude, so that we fix the

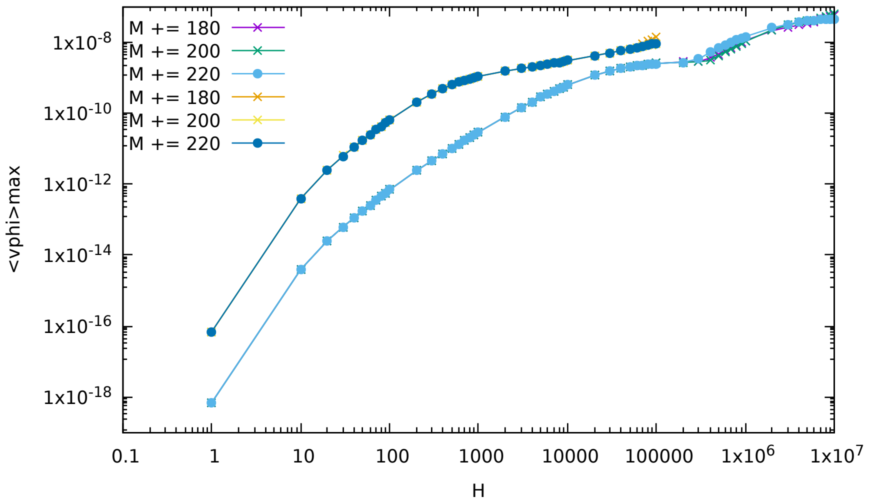

**FIGURE 14.** Maximal value of the toroidal velocity field as a function of the Hartmann number for $\eta = 6.9 \times 10^{-8}$ (upper curve) and $\eta = 6.9 \times 10^{-7}$ (lower curve). The computations have been performed for different meshes in order to check the mesh-independency of the results.

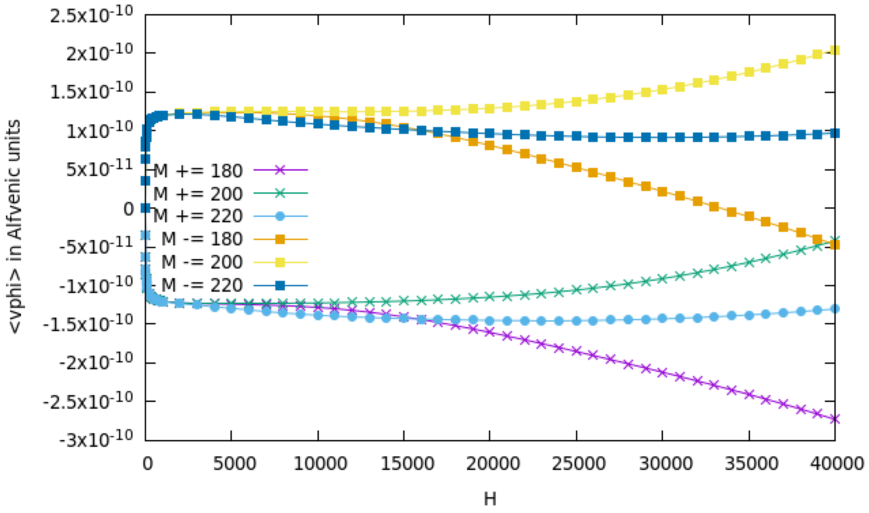

**FIGURE 15.** ITER simulations results computed with P1 elements for different meshes (M). Averages of the toroidal velocity in the upper $y \geq 0$ domain (M+) and in the lower $y \leq 0$ (M-) half of the torus.

resistivity, $\eta$, and vary the viscosity through $H$. Figures 17, 18 and 19 represent the toroidal velocity field in ITER with the same (no-slip) boundary conditions as in JET for respectively, $H = 10$, $H = 100$ and $H = 10^4$.

## INTERPRETATION AND PERSPECTIVES OF THE RESULTS

As the resistivity strongly decreases with plasma temperature, the resistivity in ITER is expected to be smaller than in JET and, for a given Hartmann number, the maximal toroidal velocity increases when the resistivity decreases. This is expected to be a favorable effect for plasma confinement. In particular, from the above numerical results, it is clear that the boundary layer regime emerges at smaller Hartmann numbers for smaller values of the resistivity. One can observe four vortices in the cross-section of the toroidal velocity field for $H = 1000$ with JET parameters whereas this

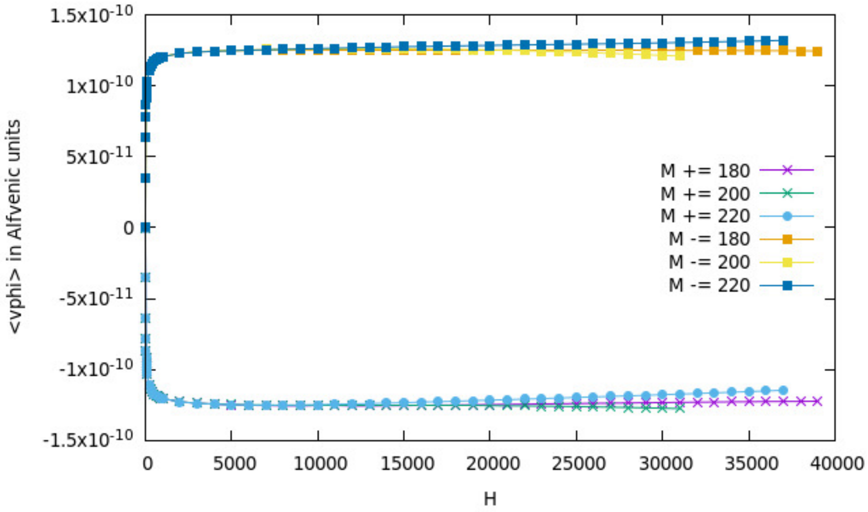

**FIGURE 16.** Same as Figure 15 using P2 elements instead of P1.

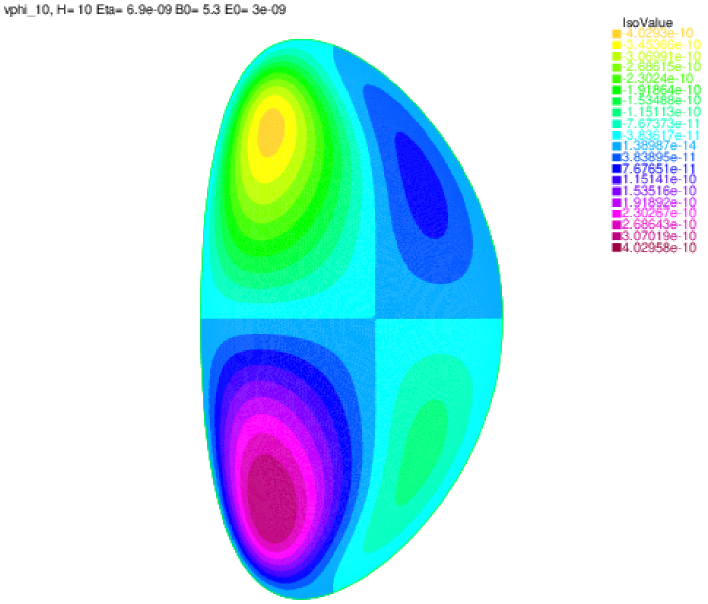

**FIGURE 17.** Toroidal velocity field computed with P2 elements in the ITER geometry for $H = 10$ with mesh adaptation on the border, other parameters are set to $E_0 = 3.10^{-9}$, $B_0 = 5\text{T}$, $\eta = 6.9 \times 10^{-9}$.

regime disappears for $H$ of the order of 10 with ITER parameters.

There is another favorable effect for ITER due to its larger plasma elongation. All other things being equal, we were able to check numerically that this geometrical factor yields an increase in the toroidal angular speed.

Nevertheless, in terms of orders of magnitude, the previous numerical results with symmetric boundary conditions are in the same range as those obtained in Ref. [3]. The natural steady flows obtained in the present simulations happen to be far too small to impact plasma confinement and to account for the measured plasma intrinsic toroidal velocities of the order of some km.s$^{-1}$. Preliminary results indicate that symmetry-breaking boundary conditions may offer a way to alleviate this problem. This will be addressed in a forthcoming publication.

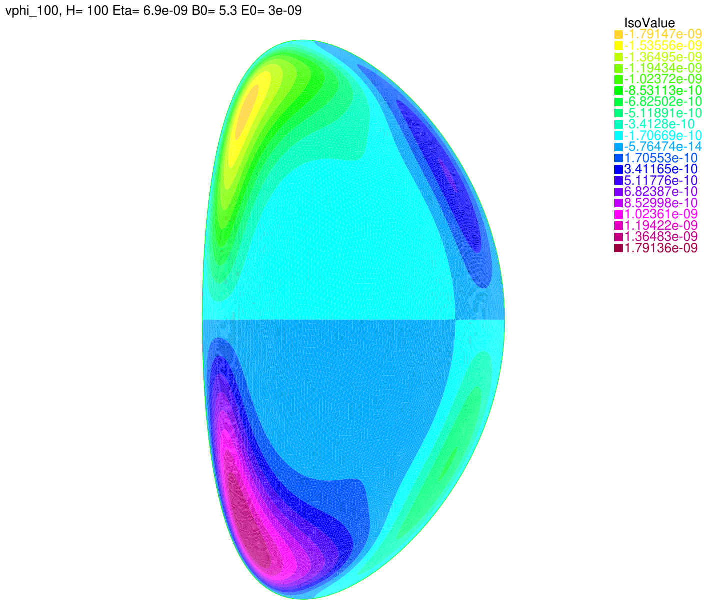

**FIGURE 18.** Same as in Figure 17 for $H = 100$.

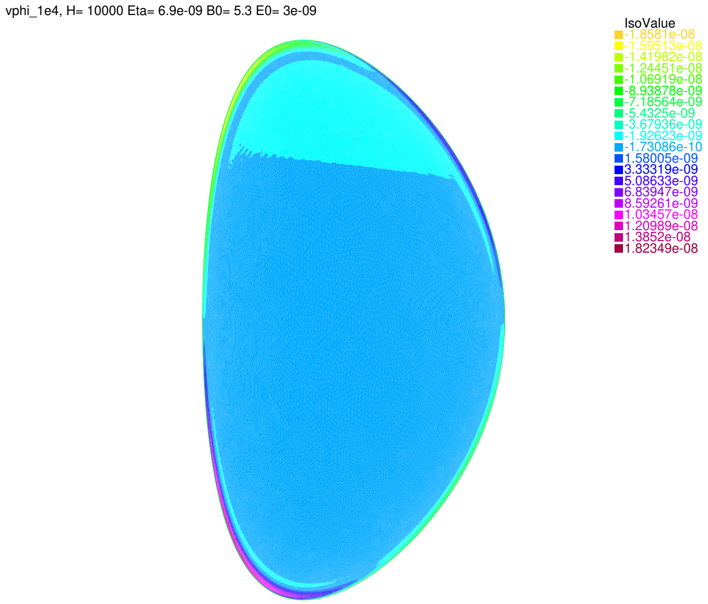

**FIGURE 19.** Same as in Figure 17 for $H = 10^4$.

## ACKNOWLEDGMENTS

This work has been performed in the frame of the FR-FCM (Fédération nationale de Recherche Fusion par Confinement Magnétique - ITER).

# REFERENCES

1. S. Friedlander and M. M. Vishik, “On stability and instability criteria for magnetohydrodynamics,” Chaos: An Interdisciplinary Journal of Nonlinear Science **5**, 416–423 (1995), https://doi.org/10.1063/1.166112.
2. D. Montgomery, J. W. Bates, and S. Li, “Toroidal vortices in resistive magnetohydrodynamic equilibria,” Physics of Fluids **9**, 1188–1193 (1997), https://doi.org/10.1063/1.869206.
3. L. P. Kamp and D. C. Montgomery, “Toroidal flows in resistive magnetohydrodynamic steady states,” Physics of Plasmas **10**, 157–167 (2003), https://doi.org/10.1063/1.1524629.
4. F. Hecht, “New development in freefem++,” J. Numer. Math. **20**, 251–265 (2012).
5. M. G. Larson and F. Bengzon, “The finite element method in 2d,” in *The Finite Element Method: Theory, Implementation, and Applications* (Springer Berlin Heidelberg, Berlin, Heidelberg, 2013) pp. 71–111.
6. L. P. Kamp, D. C. Montgomery, and J. W. Bates, “Toroidal flows in resistive magnetohydrodynamic steady states,” Phys. Fluids **10** (1998).
7. T. Williams, C. Kelley, and many others, “Gnuplot 4.6: an interactive plotting program,” `http://gnuplot.sourceforge.net/` (2014).
8. H.-T. Kim, A. C. C. Sips, P. C. de Vries, and J.-E. Contributors, “Plasma burn-through simulations using the DYON code and predictions for ITER,” Plasma Physics and Controlled Fusion **55**, 124032 (2013).
9. L. Spitzer, *Physics of fully ionized gases* (Interscience Publishers, 1956).
10. Y. Gribov, D. Humphreys, K. Kajiwara, E. Lazarus, J. Lister, T. Ozeki, A. Portone, M. Shimada, A. Sips, and J. Wesley, “Chapter 8: Plasma operation and control,” Nuclear Fusion **47**, S385 (2007).